Electronic Supplementary Information

Probing the Host-Dopant Interactions in Conducting Polymers

for Improved Electrochemical Deionization Performance

Hung-Yi Huang, Yi-Heng Tu, Yu-Hsiang Yang, Yi-An Chen, Wei-Lin Lee,

Meng-Fei Wu, Ho-Hsiu Chou, Chi-Chang Hu*

Laboratory of Electrochemistry and Advanced Materials

Department of Chemical Engineering

National Tsing Hua University

Hsin-Chu 300044, Taiwan

*: Corresponding author

This supporting information includes 20 figures and 5 tables.

1. Experimental section.

1.1. Chemicals and synthesis system

The titanium sheet, sourced from Raysen Titanium Industry Co. (Taiwan), was cut into dimensions of 1 cm × 6.5 cm for further use. The pyrrole monomer was purchased from Aldrich (USA), sodium dodecylbenzene sulfonate (SDBS) was obtained from Seedchem, and lithium perchloride (LiClO$_4$), sodium styrene 4-sulfonate (SS), and sodium 4-hydroxybenzene sulfonate (SHBS) were acquired from Alfa Aesar.

In the three-electrode system, the working electrode consisted of a pretreated titanium sheet, while the counter electrode was a platinum wire, and a commercial Ag/AgCl served as the reference electrode. The electropolymerization process employed the galvanostatic mode with the current density of the positive electrodes fixed at 4.7 mA cm^{-2} for a specific time range of 5-20 min, and the mass loading is maintained within the range of 5-12 mg.

1.2. Material characterization of PPy electrodes with dopants

The elemental composition and the actual doping ratio of PPy electrodes were confirmed by elemental analysis (EA, Vario EL cube, Elementar). The surface morphologies and hydrophilicity of various PPy electrodes were observed using a field-emission scanning electron microscope (FESEM, Hitachi SU-8010) and contact angle measurements (FTA-100B, First Ten Ångstrom). The X-ray diffraction (XRD, Bruker,

$\lambda = 1.5406$ Å) was used to examine the clustering and localized ordering of PPy films doped with various dopants. To further identify the compositions and to probe the oxidation state of PPy electrodes, Raman spectroscopy (Thermo Scientific DXR Raman Microscopy, $\lambda = 532$ nm) and high-resolution X-ray photoelectron spectroscopy (HRXPS, ULVAC-PHI, PHI Quantera II) were employed.

1.3. Electrochemical measurements of PPy electrodes with dopants

We selected a three-electrode system comprising a platinum wire as the counter electrode and a commercial Ag/AgCl as the reference electrode to investigate the electrochemical properties of various PPy electrodes with different doping ratios. Linear sweep voltammetry (LSV) was used to analyze the effect of dopants in the coating electrolyte on the electropolymerization. Furthermore, the charge transfer capability of PPy electrodes was examined via electrochemical impedance spectroscopy (EIS) under the open circuit potential (E_{OCP}). Additionally, cyclic voltammetry (CV) was used to confirm the impact of PPy-doped with various dopants on the anion/cation exchange characteristics. All electrochemical tests were measured by a CHI 6273E electrochemical workstation (Ch Instrument).

1.4. Calculation methods

The performances of ECDI full cells are assessed by the specific salt adsorption capacity (SAC, mg g^{-1}), specific SAR (mg g^{-1} min^{-1}), average SAR (mg g^{-1} s^{-1}), and

energy consumption (EC, kWh/kg-NaCl) estimated through Eq. (1)-(4), respectively:

$$specific \quad SAC\ (\Gamma) = \frac{(C_t - C_0) \times V \times MW}{m} \tag{1}$$

$$specific\ SAR_{t_2 - t_1} = \frac{\Gamma_{t_2} - \Gamma_{t_1}}{t_2 - t_1} \tag{2}$$

$$average \quad SAR_t = \frac{\Gamma_t}{t} \tag{3}$$

$$EC = \frac{v_{charging} \times \int_0^{t_{charging}} idt + v_{discharging} \times \int_0^{t_{discharging}} idt}{3.6 \times (C_1 - C_0) \times V} \tag{4}$$

where C_0 and C_t indicate the initial concentration and the concentration at a specific

time t measured by a conductivity meter and converted to the corresponding NaCl

solution concentration through the calibration curve; V is the feed solution volume

circulated in the system; MW represents the molecular weight of NaCl (58.44 g mol^{-1}),

m indicates the total mass of active material on both positive and negative electrodes; I

and V are defined as the currents (A) and cell voltages (V) during the charge and

discharge steps.

For the long-cycle stability test, the retention of SAC (R_{SAC}) was used to evaluate

the cyclic stability of the ECDI system, which was obtained from Eq. (5):

$$R_{SAC} = \frac{SAC_i}{SAC_{max}} \tag{5}$$

where SAC_i represents the specific SAC in the ith cycle and SAC_{max} is the maximum

SAC within an individual charge/discharge segment in the entire long-cycle stability
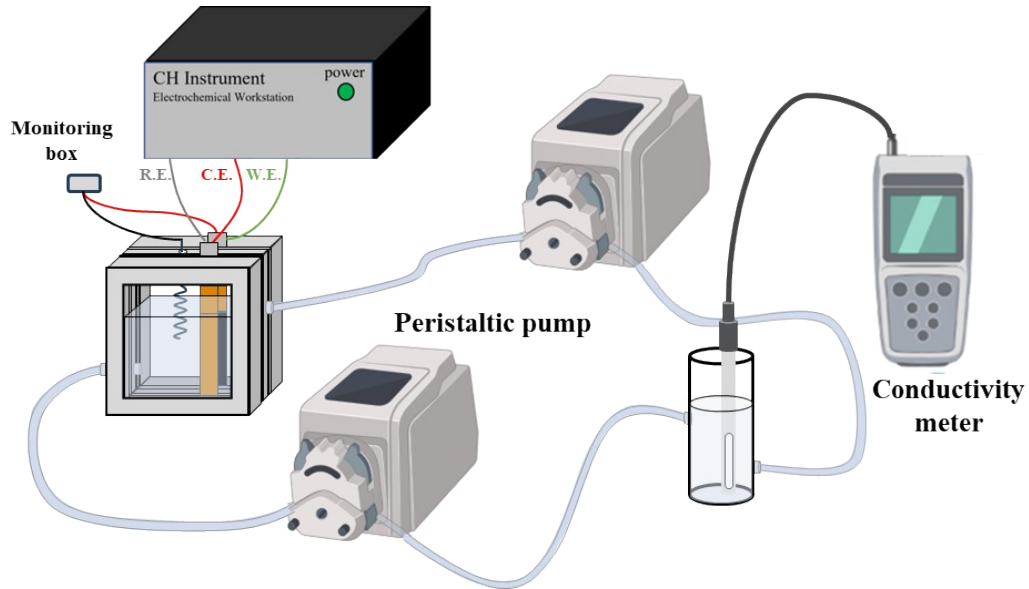
test.

Fig. S1. A schematic diagram of the flowing-by ECDI system.

Table S1. Elemental analysis of PPy-DBS-1, PPy-SS-1, and PPy-HBS-1 electrodes, comprising weight ratios of N, C, H, O, and S. The electrolyte S/N molar ratio represents the molar ratio of pyrrole monomer and dopant in the coating electrolyte.

Sample	N%	C%	H%	O%	S%	Electrolyte S/N molar ratio	Actual S/N molar ratio
PPy-DBS-1	7.78	68.09	7.32	8.38	8.04	0.5	0.45
PPy-SS-1	10.37	59.93	4.19	17.68	7.89	0.5	0.33
PPy-HBS-1	10.72	54.82	3.88	14.25	6.63	0.5	0.27

Table S1 provides the results of the elemental analysis of the PPy electrodes with various dopants. Meanwhile, to assess the doping efficiency of different kinds of benzenesulfonate analogues, the sulfur/nitrogen (S/N) molar ratio is deduced according to Eq. (6):[1]

$$\text{S/N molar ratio} = \frac{S \ in \ the \ PPy - doped \ electrode \ (mole)}{N \ in \ the \ PPy - doped \ electrode \ (mole)} \quad (6)$$

The results indicate the substantial variation in the doping efficiency among different
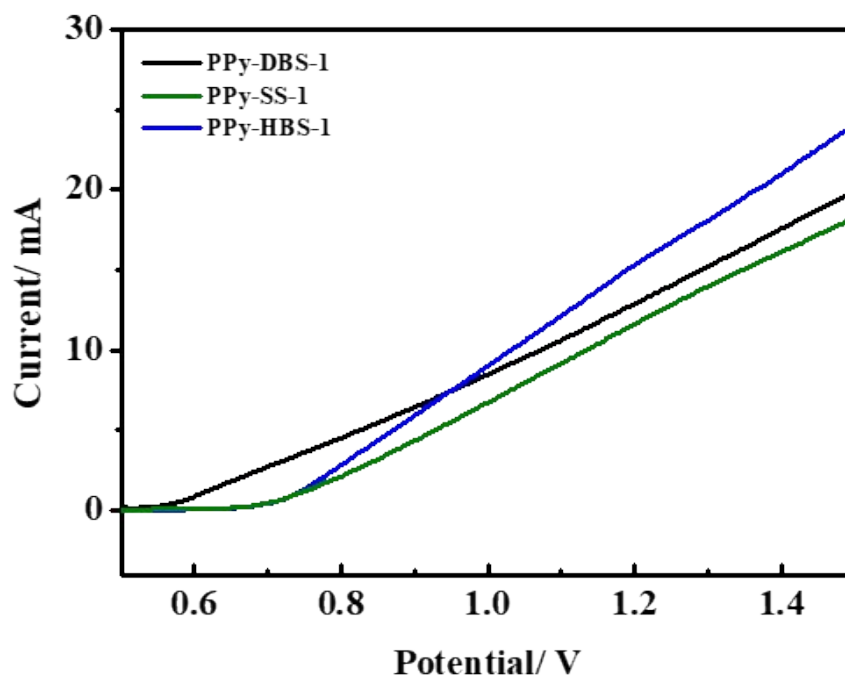
dopants in the PPy electrodes.

Fig. S2. LSVs measured at 2 mV s^{-1} in the electropolymerization electrolytes for
preparing the PPy-DBS-1, PPy-SS-1, and PPy-HBS-1 electrodes.

Fig. S2 shows the LSVs measured in the electropolymerization electrolytes for

preparing various PPy electrodes to visualize the impact of dopants on the doping

efficiency under the same dopant concentration of coating electrolytes. The results

show that the overpotential of the three electrodes follows the tendency which is

consistent with their respective actual doping efficiencies. Moreover, it is also observed

from the LSVs that DBS acts as a surfactant and enables the monomer to disperse more

uniformly in the aqueous solution, resulting in the lowest onset potential of the

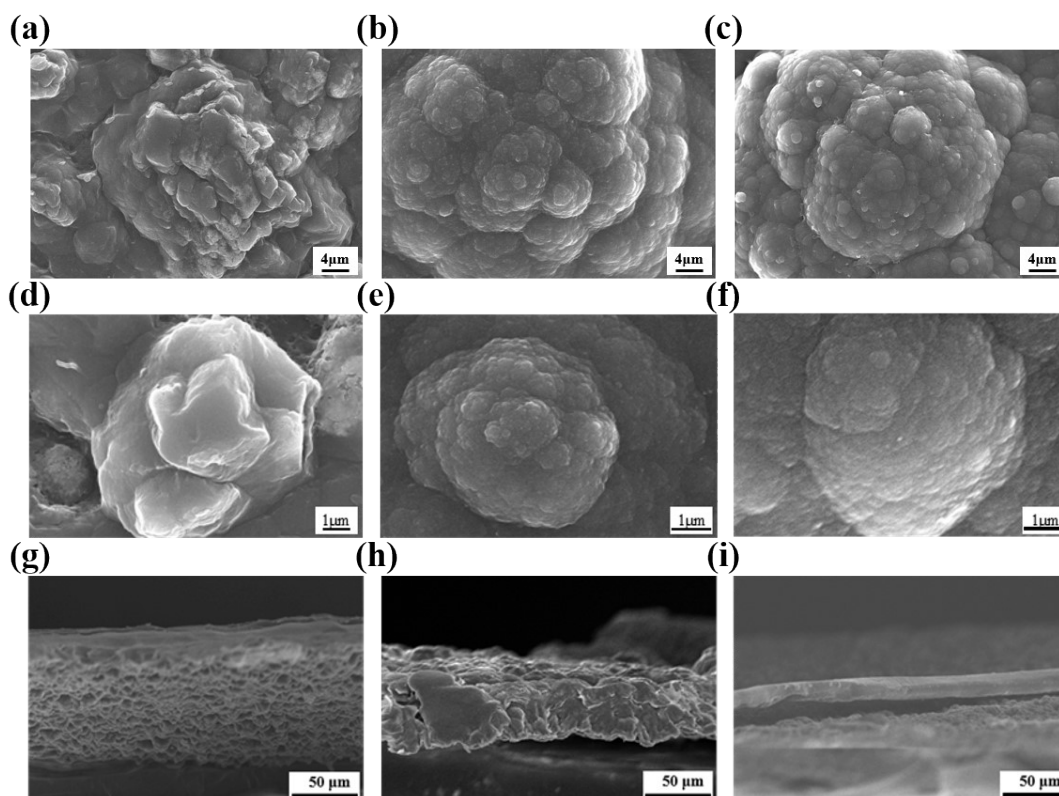electropolymerization as well as achieving the highest doping efficiency.

Fig. S3. (a-c) Low-magnification, (d-f) high-magnification, and (g-i) cross-section SEM images of (a, d, g) PPy-DBS-1, (b, e, h) PPy-SS-1, and (c, f, i) PPy-HBS-1 electrodes at the same S/N molar ratio in the coating electrolytes.
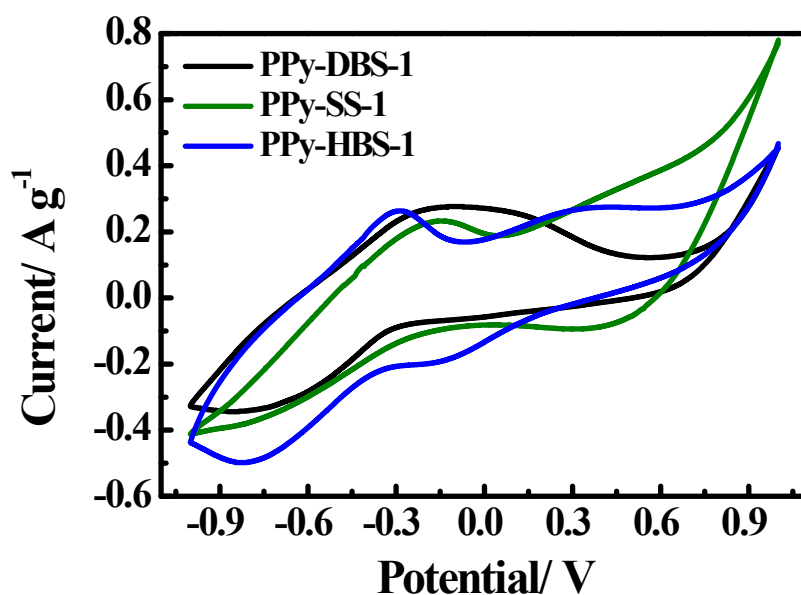

Fig. S4. The CVs measured in 10 mM NaCl at a scan rate of 2 mV s^{-1} for the PPy doped with various dopants at the same S/N molar ratio. Potential is reported against an Ag/AgCl wire.

Table S2. Assignments of the Raman bands of PPy-DBS-1, PPy-SS-1, and PPy-HBS-1 electrodes based on the data in the literature.

Species	Symbol	Wavenumber / cm⁻¹	Assignment	Ref.
Neutral	a	922,983	C-C ring deformation (neutral)	2
Polaron	b	940	C-C ring deformation (protonated)	3
Both	c	967	C-C ring deformation	3
Both	d	1050	C-H in-plane deformation with neutral PPy	4
Polaron	e	1084	C-H in-plane deformation with oxidized PPy	2
Polaron	f	1227	N-H bending vibration	5
Neutral	g	1318	C-H stretching of neutral PPy	4
Polaron	h	1377	antisymmetric inter-ring stretching C-N vibration	6
Both	i	1571	C=C vibration in the pyrrole ring	7

Based on Table S2, the vibrational energy bands below 1100 cm⁻¹ were expected to contain ring in-plane deformation and C-H in-plane bending vibration. In the case of the non-protonated (neutral) PPy segment, the corresponding ring deformation band occurred at 922 cm⁻¹, while the protonated PPy segment occurred at 940 and 967 cm⁻¹. The C-H in-plane bending vibrations were assigned to the double bands observed at

1050 and 1084 cm^{-1}. The band at the higher frequency side was attributed to the C-H in-plane deformation with oxidized PPy and confirmed the presence of polaron in the doped PPy, while the lower band corresponded to the neutral PPy. The vibrational energy bands in the range of 1100-1700 cm^{-1} were expected to have three types of molecular vibration, including N-H in-plane bending,[5] backbone C-C stretching,[4] and backbone C=C stretching.[8, 9] The double bands located at 1318 and 1377 cm^{-1} were attributed to the backbone C-C stretching of PPy, with the higher band assigned to the antisymmetric inter-ring stretching C-N vibration of the oxidized PPy, and the lower band assigned to the C-H stretching of the neutral PPy. The intensity of the former band was observed to increase as the PPy chain became deprotonation, showing an inverse correlation with the doping efficiency.

Table S3. The deconvolution details of the XPS N1s core level spectra corresponding to various types of PPy-doped electrodes.

Sample	Baseline method	Peak binding energy (eV)	FWMH (eV)	Area
PPy-DBS-1	Tougaard method	401.088	1.98075	2222.43
		399.423	1.61899	490.21
PPy-SS-1		399.405	1.97447	3004.998
		397.157	1.37434	157.28
PPy-HBS-1		399.287	1.94312	1955.91
		397.396	1.03582	179.67
PPy-SS-2		401.346	1.85346	1563.84
		399.492	1.73526	3469.19
PPy-HBS-2		401.188	1.73063	1012.24
		399.414	1.59209	3194.44
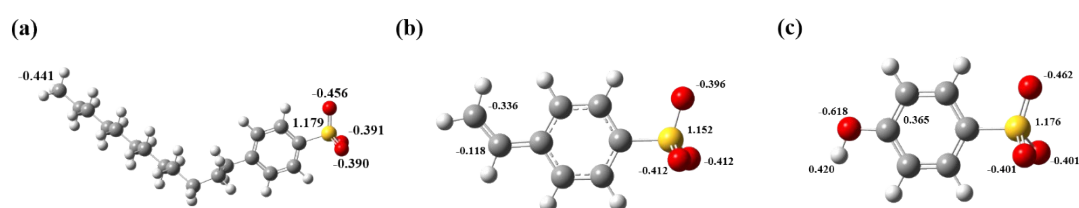
Fig. S5. Molecular structure and partial charge of (a) DBS, (b) SS, and (c) HBS via the density functional theory (DFT) at the B3LYP/6-31G* level of theory using Gaussian16.
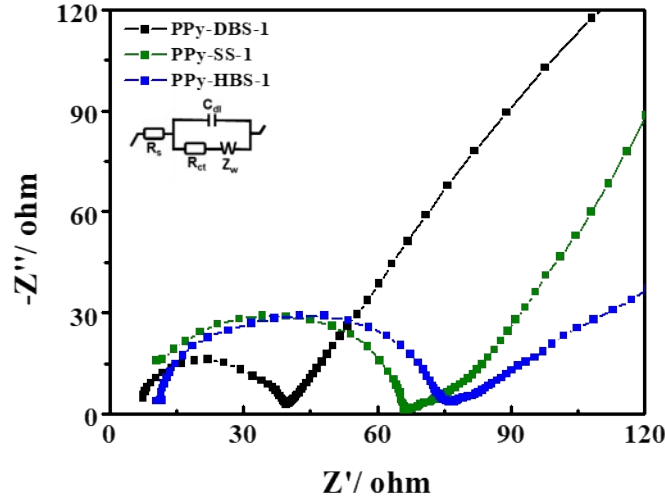
Fig. S6. EIS data of PPy-DBS-1, PPy-SS-1, and PPy-HBS-1 electrodes in 10 mM NaCl under their open-circuit potentials (E_{OCP}).

For Fig. S6, the Nyquist plot provides insights into the charge transfer and ion diffusion capabilities of various PPy electrodes. Within this plot, the semicircle observed in the high-frequency region can be attributed to the process occurring at the polymer–electrolyte interface. Specifically, it is anticipated to represent the double-layer capacitance operating in parallel with the ionic charge-transfer resistance (R_{ct}) due to the ion exchange for charge compensation at the polymer–solution interface.[10] The results indicate that the R_{ct} of the PPy-DBS-1 electrode is much smaller than those of the PPy-SS-1 and PPy-HBS-1 electrodes, in agreement with their respective average oxidation states. This finding suggests that a higher average oxidation state can enhance the charge carrier mobility of the PPy skeleton, leading to better conductivity and lower charge transfer impedance of the electrode, which effectively reduces the energy consumption of the ECDI system.
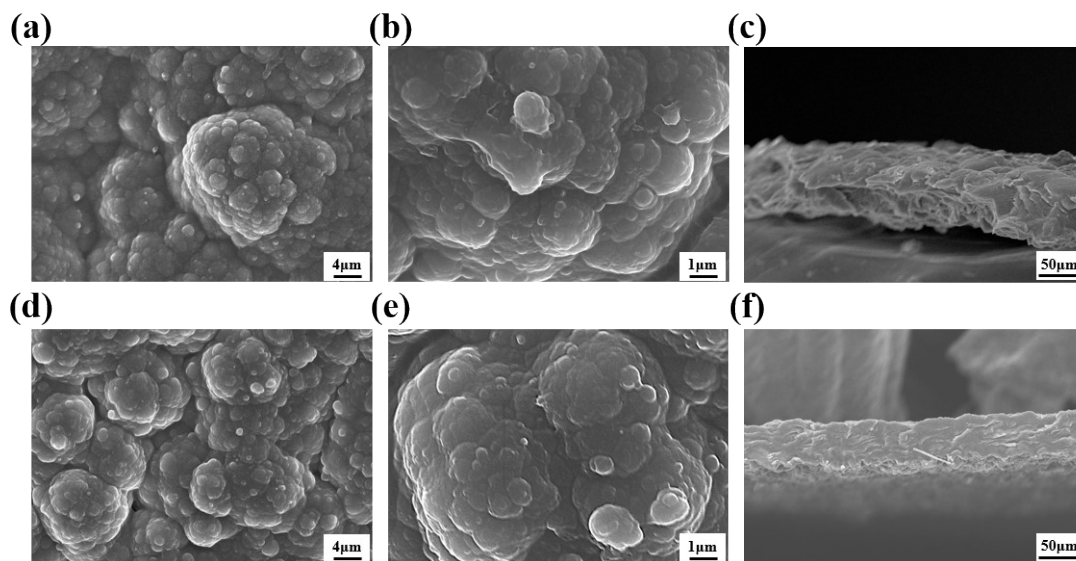
Fig. S7. (a, d) Low-magnification, (b, e) high-magnification, and (c, f) cross-section SEM images of (a-c) PPy-SS-2 and (d-f) PPy-HBS-2 electrodes at the same actual S/N ratio based on the results of elemental analysis.
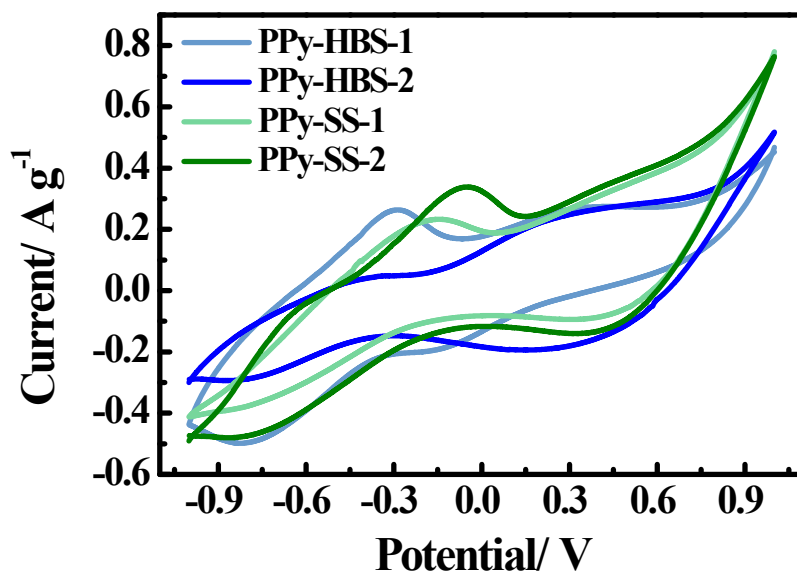

Fig. S8. The CVs measured in 10 mM NaCl at a scan rate of 2 mV s^{-1} for the PPy-HBS and PPy-SS electrodes with different actual S/N ratios. Potential is reported against an Ag/AgCl wire.
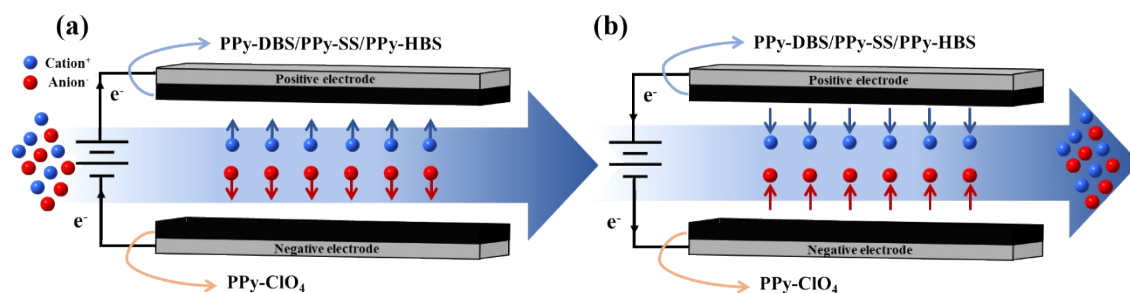
Fig. S9. The deionization mechanism of PPy-doped ECDI system during (a) discharging (ions-removal) step and (b) charging (ions-released) step.
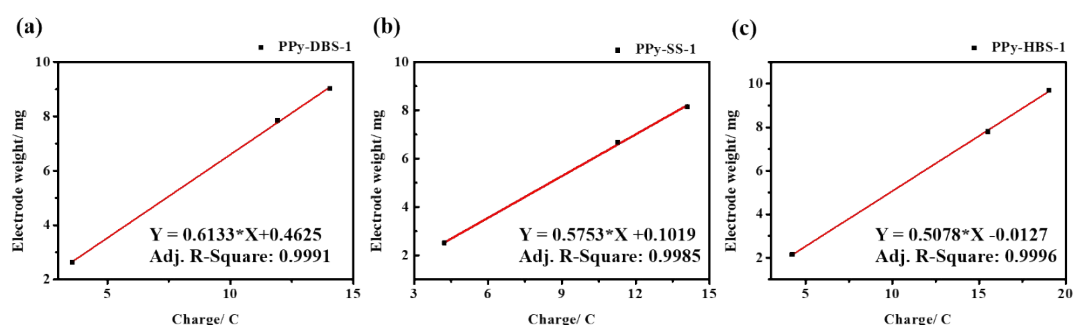

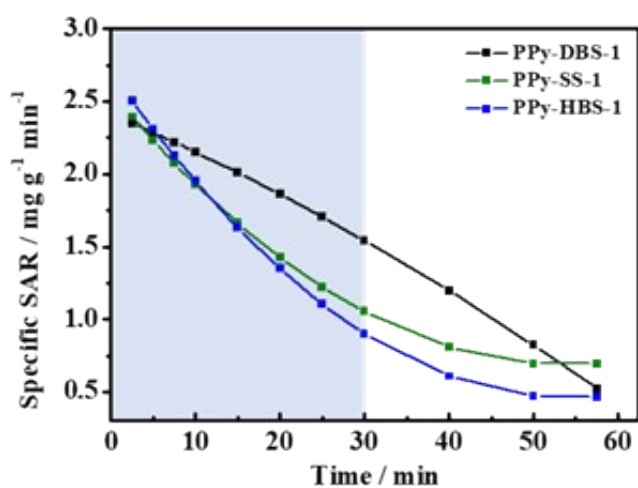Fig. S10. Calibration curves of mass *vs.* charge for (a) PPy-DBS-1, (b) PPy-SS-1, and (c) PPy-HBS-1 electrodes.

Fig. S11. Evolution of specific SAR over time in the discharge processes for the PPy-DBS-1//PPy-ClO$_4$, PPy-SS-1//PPy-ClO$_4$, and PPy-HBS-1//PPy-ClO$_4$ systems with the optimized operating parameters (including mass loading ratio and charge/discharge voltages).

From Fig. S11, in the discharge process, all three systems exhibit comparable SAR values within the initial 10 min due to the facile active site utilization near the superficial region of all PPy-based electrodes. Subsequently, between 10 and 60 min, the PPy-DBS-1//PPy-ClO$_4$ system showed the highest average SAR and the slowest decay rate of specific SAR among the three cells. This trend can be primarily attributed to the differences in the microstructure of conducting polymers. The larger d-spacing effectively enhances the transportation efficiency of hydrated and partially hydrated sodium ions, resulting in the higher utilization of PPy-DBS-1 and the highest desalination capability of PPy-DBS-1//PPy-ClO$_4$. Moreover, the PPy-SS-1//PPy-ClO$_4$ system showed a higher average SAR value in the long-term operation than the PPy-HBS-1//PPy-ClO$_4$ system due to the difference in the doping efficiency between SS and HBS although the specific SAR of both systems displayed similar trends in the specific SAR.
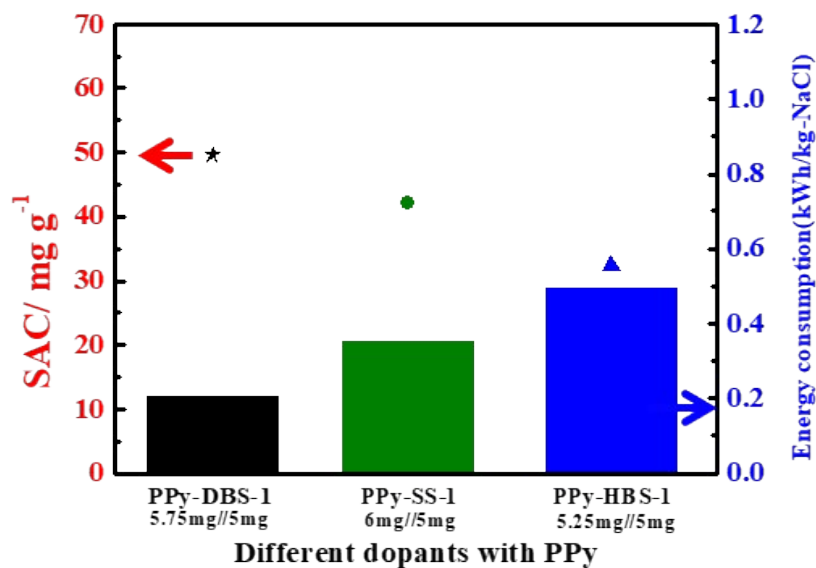
Fig. S12. The plot of SAC and energy consumption for various ECDI systems at fixed operating parameters (including mass loading of the negative electrode (= 5 mg), mass loading ratio, charge/discharge times, and charge/discharge voltages) with the same S/N molar ratio in the coating electrolytes.
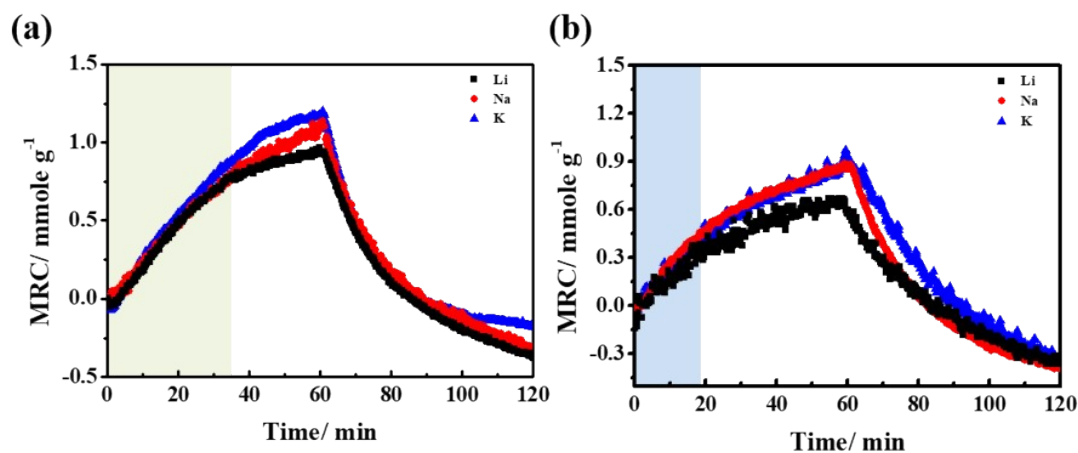

Fig. S13. The SAC profiles in (a) PPy-DBS-1//PPy-ClO$_4$ and (b) PPy-HBS-2//PPy-ClO$_4$ systems at the fixed operation parameters in 10 mM LiCl, NaCl, and KCl solutions.

Fig. S13(a) illustrates that for the PPy-DBS-1//PPy-ClO$_4$ system, the efficiency of removing the three cations is comparable during the initial 40 min of discharge, and the removal efficiency of lithium ions with a larger hydrated radius (3.82 Å) only slightly

decreases at the discharge time exceeding 40 min. This suggests that the PPy-DBS-1

electrode has a lot of pathways for hydrated cations to move, and the system ability to

remove monovalent cations does not differ significantly when the charge and discharge

times are regulated. In contrast, Fig. S13(b) indicates that the PPy-HBS-2//PPy-ClO$_4$

system exhibits similar removal abilities for Na and K ions, but Li ions are hardly

removed at discharge times exceeding 20 min. This phenomenon suggests that active

sites within the PPy-HBS-2//PPy-ClO$_4$ system are not accessible to the large hydrated
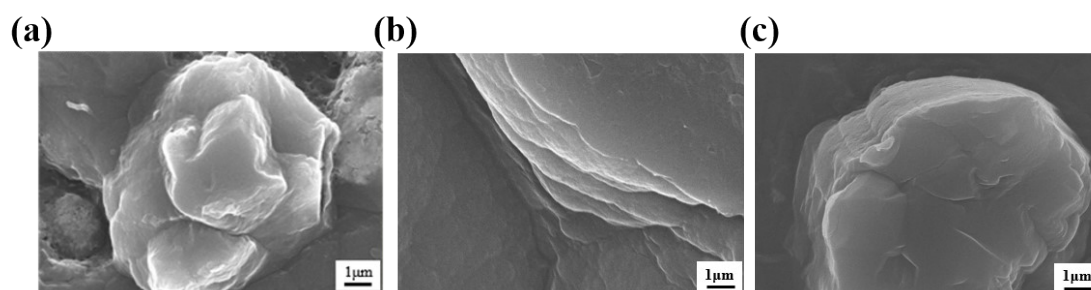
cations.

Fig. S14. The high-magnification SEM images of (a) PPy-DBS-1, (b) PPy-DBS-2, and (c) PPy-DBS-3 electrodes at the S/N ratios of 0.5, 0.4, and 0.65, respectively.
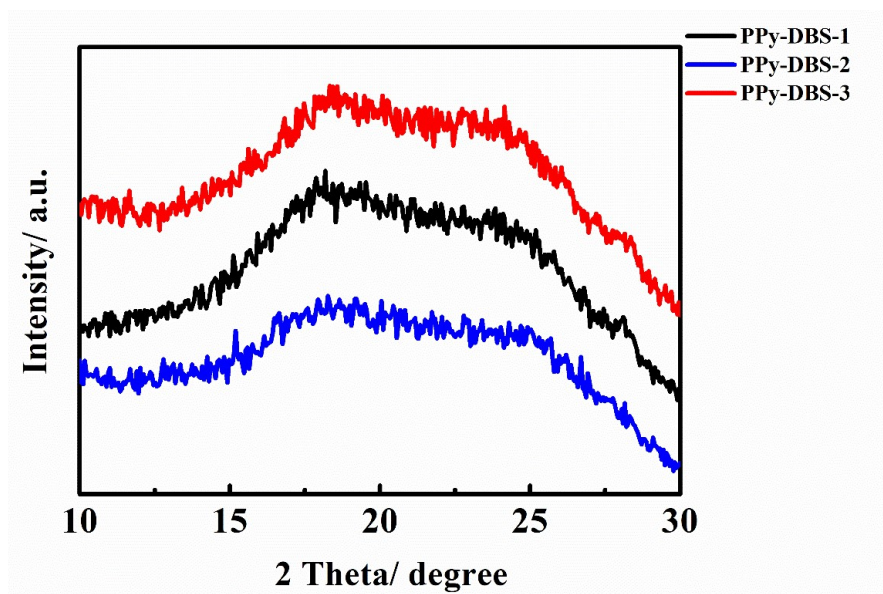
Fig. S15. X-ray diffraction patterns of PPy-DBS-1, PPy-DBS-2, and PPy-DBS-3 electrodes with the actual S/N ratios equal to 0.5, 0.4, and 0.65, respectively.
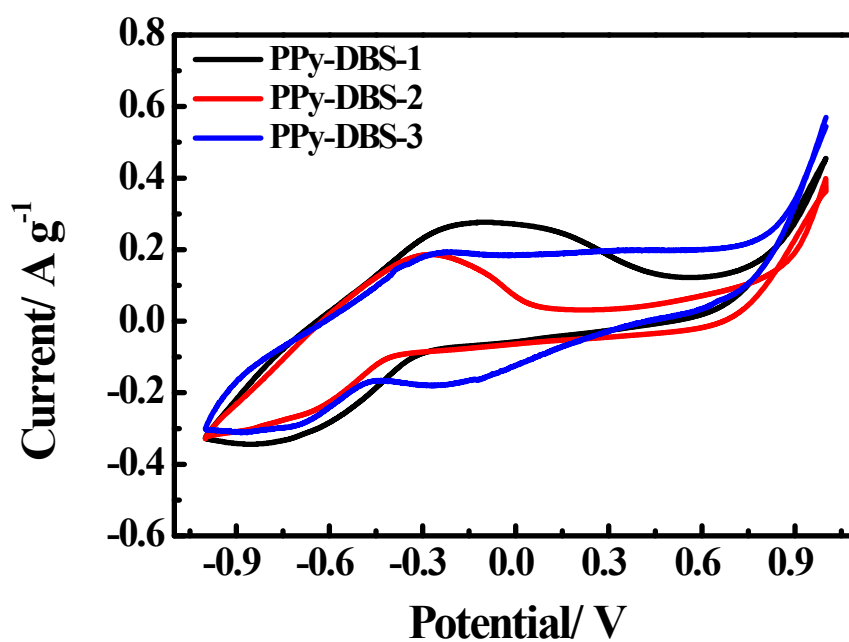

Fig. S16. The CVs measured in 10 mM NaCl at a scan rate of 2 mV s^{-1} for the PPy-DBS electrodes with different actual S/N ratios. Potential is reported against an Ag/AgCl wire.
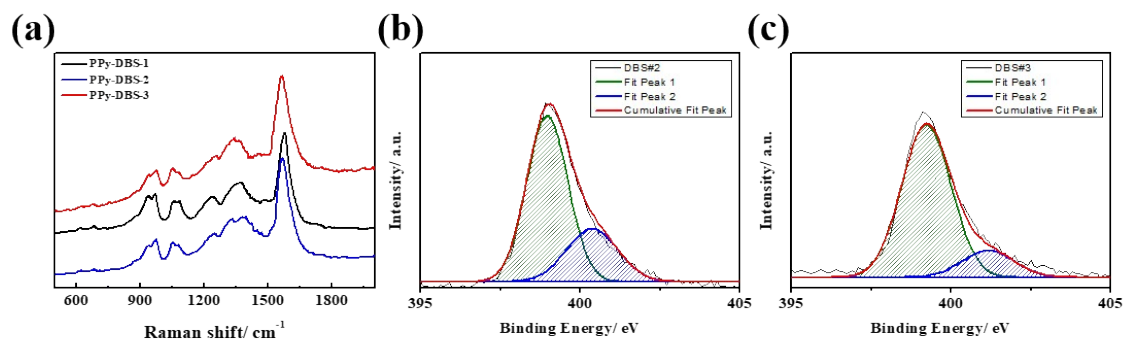
Fig. S17. (a) The Raman spectra for the PPy-DBS electrodes with the actual S/N ratios equal to 0.4, 0.5, and 0.65. The XPS N1s core level spectra of (b) PPy-DBS-2 and (c) PPy-DBS-3 electrodes.

Table S4. Comparisons of the SAC, SAC retention, and cycle number performance among various high-stability ECDI systems reported in the literature.

| Electrode material	Conc./ mM	Applied voltage/ V	SAC/ mg g^{-1}	SAC retention / %	Cycle number	Ref.
KCuFe(CN)$_6$// AC	8.56	1.2	23.2	99.5	100	[11]
NP-EHPC// NP-EHPC	8.56	1.2	24.14	74	150	[12]
MXene/CNT// CNT	8.56	1.2/-1.2	34.5	89	40	[13]
CuHCF@PVA/PPy/ / AC	1000	1.2/-1.2	45	90	100	[14]
PCF//PCF	8.5	1/0	30.4	94	30	[15]
MnO$_2$//PPy-ClO$_4$	14.54	0.8/-0.8	43.2	91	50	[16]
CuHCF//PPy-ClO$_4$	8	1.2/-0.2	26.62	70	100	[17]
MnO$_2$//PPy-ClO$_4$	8	1.2/0	19	75	180	[18]
AC// MXene/BC@PPy	20	1.2/0	17.6	94.6	30	[19]
PPy-p-TS// PPy-ClO$_4$	10	0.75/-0.2	19.8	88	250	[20]
PPy-DBS-1// PPy- ClO$_4$	10	0.8/-0.7	61.7	83	50	This work
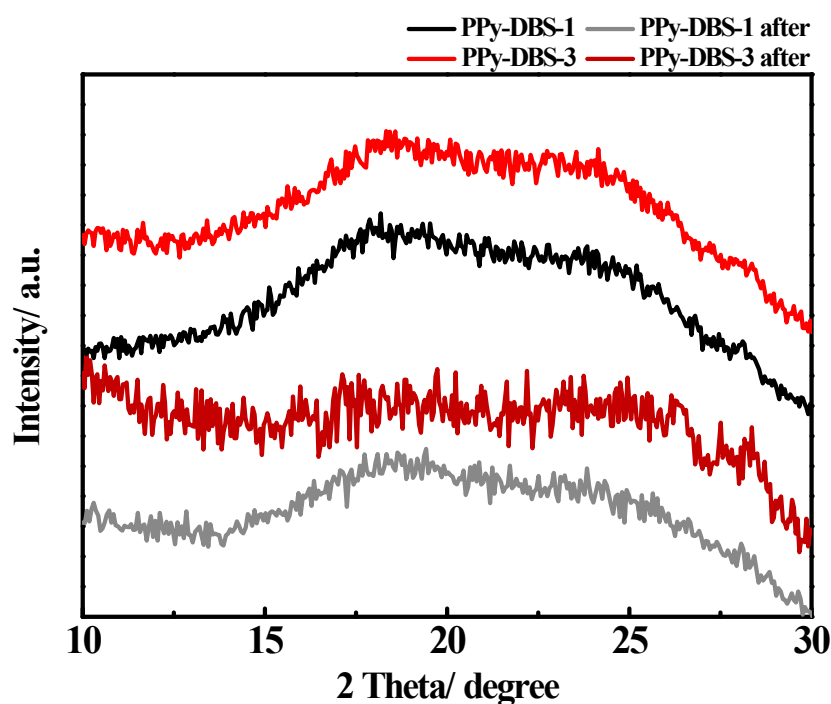
Fig. S18. Comparisons of X-ray diffraction patterns of PPy-DBS-1 and PPy-DBS-3 electrodes before and after the cycling stability test with the charge/discharge

steps at 0.8/-0.7 V and 20/30 min for 50 cycles.

Fig. S19. (a) Low-magnification, (b-c) high-magnification, and (d) cross-section SEM images of the PPy-DBS-1 electrodes after the cycling stability test with the charge/discharge steps at 0.8/-0.7 V and 20/30 min for 50 cycles.
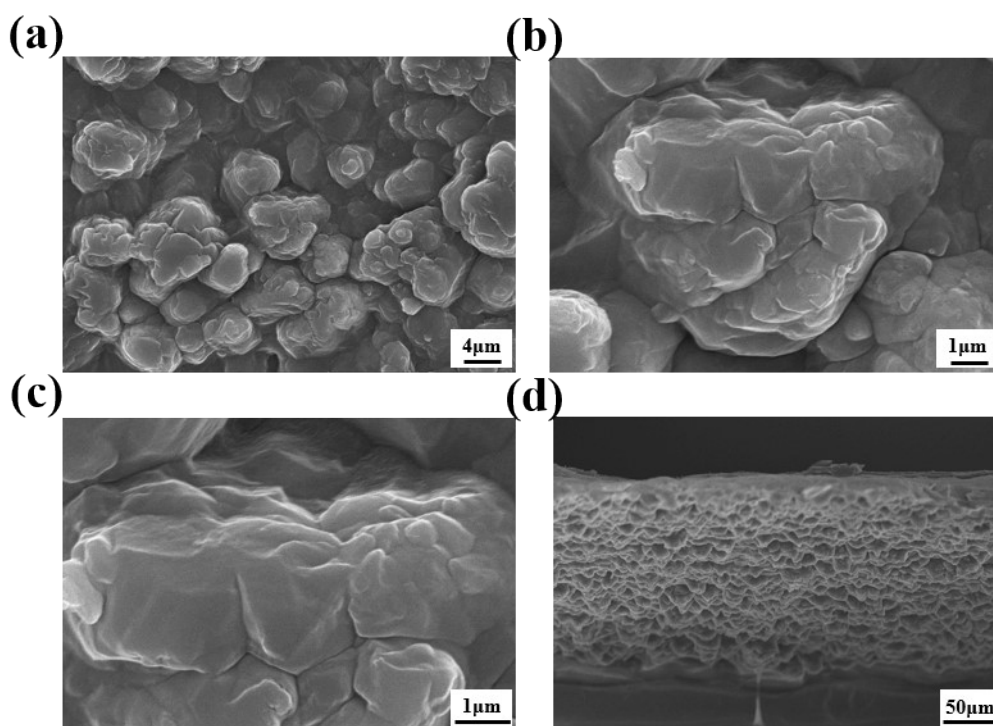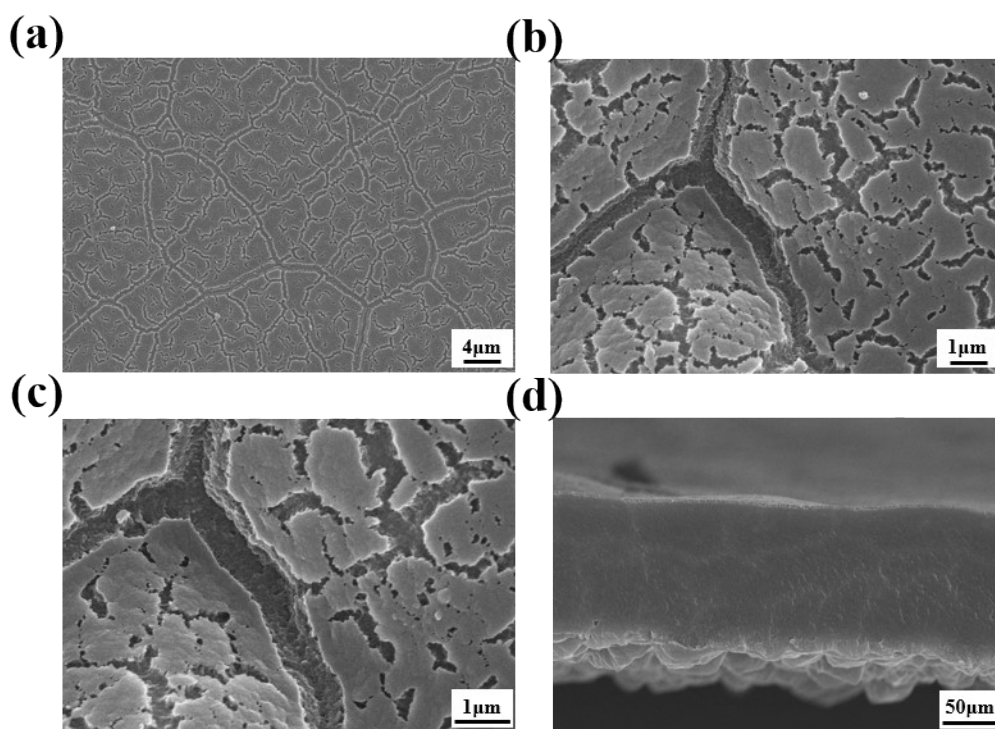

Fig. S20. (a) Low-magnification, (b-c) high-magnification, and (d) cross-section SEM images of the PPy-DBS-3 electrodes after the cycling stability test with the

charge/discharge steps at 0.8/-0.7 V and 20/30 min for 50 cycles.

Table S5. Comparisons of the SAC, average SAR, and energy consumption performance among various conducting polymer-based ECDI systems and other systems using Faradaic materials.

Electrode material	Conc./ mM	Applied voltage/ V	SAC/ mg g^{-1}	Average SAR/ mg g^{-1} s^{-1}	EC/ kWh/kg-NaCl	Ref.
Conducting polymer-based systems						
CuHCF@PVA/PPy/ / AC	1000	1.2/-1.2	45	0.01875	0.28	[14]
AC//H-NP@PANI	8.56	1.2/-1.2	35.86	0.02109	0.2263	[21]
MnO$_2$//PPy-ClO$_4$	14.54	0.8/-0.8	43.2	0.144	0.35	[16]
CuHCF//PPy-ClO$_4$	8	1.2/-0.2	26.62	0.0218	0.604	[17]
MnO$_2$//PPy-ClO$_4$	8	1.2/0	19	0.0316	0.68	[18]
AC// MXene/BC@PPy	20	1.2/0	17.6	0.01463	0.5703	[19]
PPy-p-TS// PPy-ClO$_4$	10	0.75/-0.2	38.3	0.0213	0.2225	[20]
PPy-DBS-1// PPy-ClO$_4$	10	0.8/-0.7	24.9	0.0415	0.2321	This work
			61.7	0.0342	0.2202	
			91.9	0.02553	0.1911	
Faradaic material-based systems						
PCF//PCF	8.5	1/0	30.4	0.05	0.37	[15]
PB/PANI//AC	8.56	1.4/-1.4	92	0.23	0.72	[22]
FeHCF@3DNC// FeHCF@3DNC	50	1/0	48.4	0.01344	0.41	[23]
Ti$_3$C$_2$T$_x$ MXene// Ti$_3$C$_2$T$_x$ MXene	10	1.2/-1.2	67.7	0.013	0.24	[24]
PB/rGA//AC	43	1.4/-0.2	78	0.074	0.23	[25]
MXene/CNT//CNT	8.56	1.2/-1.2	34.5	0.01725	0.283	[13]

References

1. K. S. Jang, H. Lee and B. Moon, *Synth. Met.*, 2004, **143**, 289-294.

2. F. e. Chen, G. Shi, M. Fu, L. Qu and X. Hong, *Synth. Met.*, 2003, **132**, 125-132.

3. M. Šetka, R. Calavia, L. Vojkůvka, E. Llobet, J. Drbohlavova and S. Vallejos, *Sci. Rep.*, 2019, **9**, 1-10.

4. M. Trchová and J. Stejskal, *J. Phys. Chem. A*, 2018, **122**, 9298-9306.

5. M. Grzeszczuk, A. Kępas, C. Kvarnstrom and A. Ivaska, *Synth. Met.*, 2010, **160**, 636-642.

6. J. Stejskal, M. Trchová, P. Bober, Z. Morávková, D. Kopecký, M. Vrňata, J. Prokeš, M. Varga and E. Watzlová, *RSC Adv.*, 2016, **6**, 88382-88391.

7. T.-M. Wu, H.-L. Chang and Y.-W. Lin, *Compos. Sci. Technol.*, 2009, **69**, 639-644.

8. I. Šeděnková, O. Taboubi, M. Paúrová, J. Hromádková and M. Babič, *Synth. Met.*, 2023, **292**, 117218.

9. M. Šetka, R. Calavia, L. Vojkůvka, E. Llobet, J. Drbohlavová and S. Vallejos, *Sci. Rep.*, 2019, **9**, 1-10.

10. W.-C. Chen, T.-C. Wen, C.-C. Hu and A. Gopalan, *Electrochim. Acta*, 2002, **47**, 1305-1315.

11. S. Choi, B. Chang, S. Kim, J. Lee, J. Yoon and J. W. Choi, *Adv. Funct. Mater.*, 2018, **28**, 1802665.

12. H. Zhang, C. Wang, W. Zhang, M. Zhang, J. Qi, J. Qian, X. Sun, B. Yuliarto, J. Na and T. Park, *J. Mater. Chem. A*, 2021, **9**, 12807-12817.

13. Y. Cai, L. Zhang, R. Fang, Y. Wang and J. Wang, *Sep. Purif. Technol.*, 2022, **292**, 121019.

14. Y. Ren, F. Yu, X.-G. Li, B. Yuliarto, X. Xu, Y. Yamauchi and J. Ma, *Mater. Horiz.*, 2023.

15. T. Liu, J. Serrano, J. Elliott, X. Yang, W. Cathcart, Z. Wang, Z. He and G. Liu, *Sci. Adv.*, 2020, **6**, eaaz0906.

16. G. Tan, S. Lu, N. Xu, D. Gao and X. Zhu, *Environ. Sci. Technol.*, 2020, **54**, 5843-5852.

17. Y.-H. Yang, Y.-H. Tu, H.-Y. Huang and C.-C. Hu, *Desalination*, 2023, **545**, 116160.

18. Y.-H. Tu, Y.-C. Tai, J.-Y. Xu, Y.-H. Yang, H.-Y. Huang, J.-H. Huang and C.-C. Hu, *Desalination*, 2022, **538**, 115928.

19. W. Xu, C. Tan, A. Wang, S. Hu, L. Deng, S. Boles, K. Sun, B. Li and H. Hu, *ACS Appl. Mater. Interfaces*, 2023, **15**, 16266-16276.

20. H.-Y. Huang, Y.-H. Tu, Y.-H. Yang, Y.-T. Lu and C.-C. Hu, *Chem. Eng. J.*, 2023, 141373.

21. J. Guo, Y. Wang, H. Zhang, Y. Cai and R. Fang, *Desalination*, 2023, **548**, 116305.

22. W. Shi, X. Liu, T. Deng, S. Huang, M. Ding, X. Miao, C. Zhu, Y. Zhu, W. Liu and F. Wu, *Adv. Mater.*, 2020, **32**, 1907404.

23. A. Gong, Y. Zhao, M. He, B. Liang and K. Li, *Desalination*, 2021, **505**, 114997.

24. J. Ma, Y. Cheng, L. Wang, X. Dai and F. Yu, *Chem. Eng. J.*, 2020, **384**, 123329.

25. S. Vafakhah, L. Guo, D. Sriramulu, S. Huang, M. Saeedikhani and H. Y. Yang, *ACS Appl. Mater. Interfaces*, 2019, **11**, 5989-5998.